Journal of Nuclear Materials 382 (2008) 134–142

Contents lists available at ScienceDirect

Journal of Nuclear Materials

journal homepage: www.elsevier.com/locate/jnucmat

Modeling of He–defect interactions in ferritic alloys for fusion

R.J. Kurtz *, H.L. Heinisch, F. Gao

Pacific Northwest National Laboratory, P.O. Box 999, P8-15, Richland, WA 99352, USA

A B S T R A C T

High concentrations of helium will be produced in fusion reactor structural materials due to neutron capture reactions. The creep-rupture and fracture properties may be severely degraded if helium aggregates at grain boundaries to a sufficiently high level. To design helium-resistant microstructures requires detailed knowledge of the transport and fate of helium to sinks. We utilize atomistic methods to study the fate of helium in the neighborhood of dislocations, grain boundaries and coherent nano-clusters in α-iron. The binding energies of helium to these defects are strongly correlated with excess atomic volume. Molecular dynamics and the dimer saddle point search method were employed to study the mobility of both interstitial helium atoms and helium–vacancy complexes in dislocations and grain boundaries. The migration energy of interstitial helium in these defects was found to range from about 0.4–0.5 eV.

1. Introduction

Reduced activation ferritic/martensitic steels are the leading candidate first-wall/blanket structural materials for fusion power systems [1]. In these materials He will be produced at concentrations approaching ~1800 appm at end-of-life doses of ~170 dpa [2]. Since He is essentially insoluble in metals and tends to aggregate at internal defects such as vacancy clusters, voids, dislocations, grain boundaries, lath boundaries and particle–matrix interfaces, it is essential to develop a detailed picture of He transport and fate in the complex ferritic steel microstructure. It is well known that at high-temperatures ($\geqslant 0.5\ T_{melting}$) the creep-rupture properties of steels will be significantly degraded if He is allowed to preferentially collect at grain boundaries [3]. It is also well known that the upper operating temperature limit for conventional ferritic steels is approximately 550 °C due to a rapid fall-off in tensile and creep strength with increasing temperature [1]. A more economically attractive fusion power system may be feasible if nanostructured ferritic alloys (NFA) can be developed to improve creep strength [1] and to better manage He by creating a high-density of nanoparticles to serve as obstacles to dislocation glide, as well as providing fine-scale He bubble nucleation sites and preferred locations for point defect recombination [4].

The work reported here is part of a comprehensive effort to develop a multi-scale model of He transport and fate in ferritic/martensitic alloys [5]. The model will be used to predict the performance of irradiated conventional alloys and NFA. Fundamental He effects experiments will be performed to gather key information to validate the model. Ultimately the validated model will be used to develop high-performance NFA for fusion. We highlight recent atomistic results of modeling the binding and migration of He at extended defects in Fe such as dislocations, grain boundaries (GB), and particle–matrix interfaces. Our interest here is to identify generic properties of these microstructural features that control the binding and migration of He. Consequently we employ a wide variety of atomic-scale computational tools to investigate the effects of dislocation character, GB structure, and particle–matrix elastic property mismatch on the binding and migration of He in and near these defects.

2. Computational methods

2.1. Interatomic potentials

In principle, *ab initio* simulations provide the most realistic approach to computational modeling of atomic-scale phenomena in crystalline materials. However, being restricted to atom configurations that comfortably fit within extremely small volumes and can be made to have periodic boundary conditions, renders an *ab initio* approach unfeasible for our present studies of He interactions with extended defects such as dislocations, grain boundaries and particle–matrix interfaces. On the other hand, molecular dynamics (MD) using interatomic potential functions suffers from a lack of realistic interatomic interactions, simply because much of the important physics of the interactions cannot be directly included. However, because of the large size of models that can be dealt with relatively efficiently, MD models can easily be applied to situations that include long-range fields and the essential features of large, non-symmetric defected regions of the material.

Thus, a set of interatomic potentials for Fe–Fe, Fe–He and He–He interactions suitable for use in MD simulations is needed for

* Corresponding author. Tel.: +1 509 373 7515; fax: +1 509 376 0418.
E-mail address: rj.kurtz@pnl.gov (R.J. Kurtz).

0022-3115/$ - see front matter © 2008 Elsevier B.V. All rights reserved.
doi:10.1016/j.jnucmat.2008.08.020

these studies. In recent years a number of MD simulations of radiation damage and defect interactions in α-Fe, as well as studies of the properties of He in Fe, have been performed using the same set of interatomic potentials [6–10]. This set consists of the Finnis–Sinclair type potential for Fe–Fe due to Ackland et al. [11], the Wilson and Johnson potential for Fe–He [12], and the He–He potential used by Beck [13]. Thus, for consistency in comparing our present simulations of He in grain boundaries and dislocations to the body of earlier work, we have used this set of potentials in the present simulations.

The Ackland et al. Fe–Fe potential, has a functional form with parameters that can be fitted to the values of a set of material properties (usually for the perfect crystal and often to some defect properties, such as vacancy and interstitial formation energies) determined numerically by experimental measurements or *ab initio* calculations. However, there is no guarantee that this potential or any other existing interatomic potentials for Fe can adequately represent all non-equilibrium or non-symmetric atom configurations of interest.

More recently, Mendelev et al. [14] developed several similar interatomic potentials for the Fe–Fe interactions that were fitted to specific properties of both crystalline and liquid Fe based on measured and *ab initio*-calculated properties. These potentials are on average in better agreement with those properties than the Ackland potential and other potentials for Fe. Of this set, the Mendelev potential #2 appears to be the best for computation of defect properties of interest to the present study. In addition to performing the calculations for all the configurations addressed in this paper using the Ackland potential, we have also calculated the formation energies of octahedral and tetrahedral interstitial He in Fe using the Mendelev #2 Fe–Fe potential for comparison. The formation energies of He in the octahedral and tetrahedral interstitial configurations are 5.25 and 5.34 eV, respectively, using the Ackland potential, while the corresponding values using the Mendelev potential are 4.99 and 5.13 eV. The *ab initio* values [15,16] are 4.57–4.60 and 4.37–4.39 eV. The results with the Mendelev potential are somewhat closer numerically to the *ab initio* values, but they also do not predict that the tetrahedral configuration has the lower formation energy.

Recently Seletskaia et al. [17] developed a new Fe–He potential that more accurately reproduces the *ab initio* interstitial and substitutional He formation energies in Fe. This Fe–He potential correctly gives tetrahedral interstitial He a lower formation energy than octahedral interstitial He, but the energy difference between these two configurations is only 0.04 eV compared to *ab initio* values of 0.18–0.23 eV [15,16]. The Wilson Fe–He potential predicts a small energy difference between the octahedral and tetrahedral interstitial sites (0.09 eV), but incorrectly gives the lowest formation energy for the octahedral site. The consequences of these differences are likely not significant given our primary interest here, which is the behavior of He in microstructural defects that deviate substantially from a perfect Fe lattice. Nevertheless, in the future, we plan to test the sensitivity of our results to the choice of interatomic potential by repeating selected simulations using the more recently developed Fe–Fe and Fe–He potentials.

An objective of our work is to explore the effect of particle elastic properties on binding of He–vacancy clusters to particle–matrix interfaces. Coherent, nanometer-scale particles with elastic constants both stiffer and softer than Fe were examined in this study. We selected the Cu–Cu and Fe–Cu interatomic potentials developed by Ackland et al. [11] to model coherent bcc particles possessing elastic properties stiffer than Fe. To explore the situation when particle elastic properties are softer than Fe we modified the above potentials so that the lattice parameter and cohesive energy for modified Cu were nearly the same as for real Cu, but the elastic constants were significantly decreased to c_{11} = 100 GPa, c_{12} = 75.4 GPa and c_{44} = 35.3 GPa. We basically followed the same procedure described by Ackland et al. [11] to construct the modified Cu–Cu and Fe–Cu potentials. Important physical properties for the suite of Fe–Cu–He potentials employed in this work are given in Table 1.

2.2. Excess volume of extended defects

The results of our simulations show that the availability of excess volume within and near lattice defects strongly influences the disposition of He in crystalline materials. The atomic volume is defined as the locus of all points in space surrounding an atom that are closer to that atom than to any other atom. 'Excess volume' at a location in an imperfect lattice can be defined in terms of the deviation of the atomic volume at that location from the atomic volume at a similar location in a perfect lattice. Thus, by this definition, there is no excess volume in a perfect lattice. We define two manifestations of excess volume that are closely related: 'excess atomic volume' centered on lattice sites and 'excess interstitial volume', which can be considered as a measure of the same overall excess volume, but defined relative to the specified 'center' of an interstitial region rather than being centered on an atom. Excess interstitial volume is a particularly useful concept when dealing with interstitial He atoms within grain boundaries and in the strain fields around dislocations (where tensile strains create regions of excess interstitial volume and compressive strains create regions of deficient interstitial volume – or 'negative excess volume').

In the present work, both excess atomic volumes and excess interstitial volumes were determined using the Voronoi volume construction [18]. The Voronoi volume can be obtained by determining the volume of the polyhedron formed by the planes that are perpendicular bisectors of the lines connecting the central atom to all other atoms (typically 2–3 neighbor shells). To deter-

Table 1
Physical properties of the Fe–Cu–He Finnis–Sinclair potential and the modified Cu potential

Property	Ackland et al. Fe	Mendelev et al. Fe	Ackland et al. fcc Cu	Modified fcc Cu	Ackland et al. bcc Cu	Modified bcc Cu
Lattice parameter (nm)	0.28665	0.28553	0.3615	0.3615	0.2961	0.3041
c_{11} (GPa)	243	243	169	100	290	198
c_{12} (GPa)	145	145	122	75.4	192	103
c_{44} (GPa)	116	116	76	35.3	147	66.1
Cohesive energy (eV)	4.316	4.122	3.519	3.519	3.496	3.599
Defect formation energies (eV)						
Vacancy	1.70	1.71	1.19	1.00	1.32	1.67
Di-vacancy (1nn)	3.26	–	2.21	1.88	2.42	3.13
Di-vacancy (2nn)	3.22	–	2.42	2.00	2.55	3.19
Substitutional He	3.25	–	2.75	2.68	2.54	2.67
Octahedral interstitial He	5.25	4.99	–	–	–	–
Tetrahedral interstitial He	5.34	5.13	–	–	–	–
He_1V_2 complex (1nn)	4.49	–	3.60	3.41	3.42	3.97
He_1V_2 complex (2nn)	4.76	–	3.98	3.69	3.73	4.15

mine interstitial volumes, the center of the interstitial site was determined from the positions of surrounding atoms, and then the interstitial volume associated with that position was determined using the Voronoi construction. To determine excess volumes, the atomic and interstitial volumes in the dislocated crystal were compared to the atomic and interstitial volumes, respectively, in the perfect crystal.

2.3. Dimer method

The dimer method has been described in detail elsewhere [19], so only the central principles are provided here. The dimer method is a numerical algorithm that finds saddle points in a potential surface of arbitrarily high dimension. Basins of the potential surface correspond to metastable states of the system, and the saddle points are the lowest energy-transition points between these states. Knowledge of these saddle points enables the determination of rates of reactions involving transitions from one energy basin to another. Algorithms in the dimer method are different from the widely used nudged-elastic band method [20] for finding transition state saddle points. The nudged-elastic band requires the initial and final states of a transition to obtain the energy barriers, while the dimer method only needs the initial state. The dimer method involves working with two atomic images of the system that are displaced from each other by a small distance. To search for a saddle point involves two operations, namely rotating and translating the dimer. Each time, it is necessary to rotate the dimer towards the minimum energy, which is equivalent to finding the lowest curvature mode at the midpoint of two images, as shown in Fig. 1(a). Then, the dimer translates along this line and moves up the potential surface, as illustrated in Fig. 1(b). In the initial calculation, the dimer is minimized along a line defined by the initial force, and it is then moved a small distance along the line to calculate the derivative of the effective force. Newton's method is used to determine the position with zero effective force along the line, and the dimer is then moved to that point. A similar approach is applied for the rotation algorithm. After each translation, the dimer is reoriented and moved along a direction conjugate to the previous line minimization. By repeating these steps, the dimer converges towards a saddle point, if it exists.

2.4. Dislocations

Molecular statics relaxations of interstitial He–dislocation configurations were performed to determine the formation energies of interstitial He defects in and around edge and screw dislocations. Some MD simulations were also performed to study the short-term intermediate-range behavior of interstitial He in the dislocation core region at low temperatures. The dimer method was used to determine transition state energies and configurations of He migration paths for interstitial He atoms in and around the dislocations.

Models of the $(a/2)[1\,1\,1][\bar{1}\,\bar{1}\,2]$ edge dislocation and the $(a/2)[1\,1\,1]$ screw dislocation were each constructed using cylindrical computational cells of about 18 000 atoms, containing the dislocation along the cylinder axis and having periodic boundaries in the direction of the dislocation line, with fixed boundaries at the surface of the cylinder, see Fig. 2. To construct the dislocated cell, all atoms in the cell were displaced according to the anisotropic elastic displacement field of the dislocation. Then, with the atoms far from the center of the cylinder fixed, the interior atoms in the cell were relaxed to their equilibrium positions by a conjugate gradient method to allow the dislocation core field to develop. Depending on the specific cases, smaller cells of 2000–5000 atoms were carved out of the larger relaxed cylinders, especially for the more computationally intensive dimer searches.

To determine He defect formation energies, a He atom was placed at a specific position within the given relaxed cell and the atoms in the cell were relaxed again. The binding energy of the He defect to the dislocation is the difference between the formation energy of the interstitial He atom in the dislocation and its formation energy in a perfect crystal.

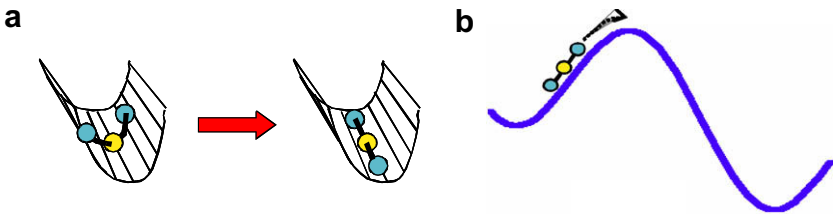

Fig. 1. Schematic diagrams showing (a) the rotation of the dimer towards the minimum energy and finding the lowest curvature mode at the midpoint of two images, and (b) the dimer translating along this line and moving up the potential energy surface.

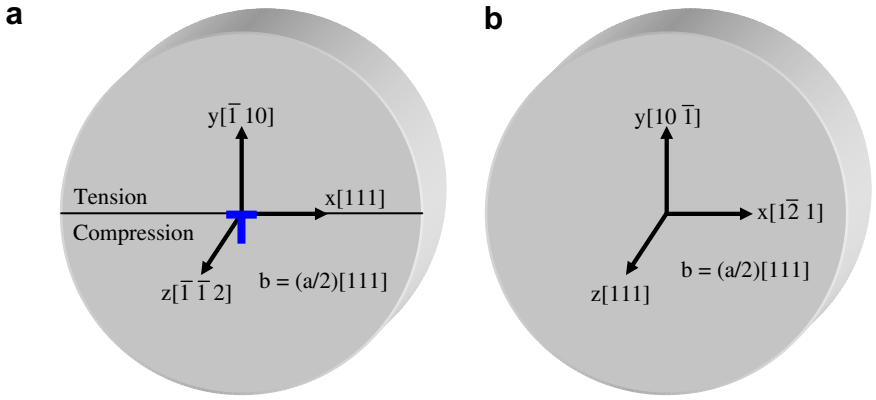

Fig. 2. Schematic drawings of the computational cells and orientations of the models of the (a) $(a/2)\langle 1\,1\,1\rangle[\bar{1}\,\bar{1}\,2]$ edge dislocation, and (b) the $(a/2)\langle 1\,1\,1\rangle$ screw dislocation.

Due to the strains associated with the dislocations, especially within the core regions, the precise locations of the tetrahedral or octahedral interstitial sites are not obvious, and the initial placement of an interstitial He atom is somewhat arbitrary. In principle, the He atom should relax to the expected equilibrium position, but in practice, during the relaxation process, some He atoms 'migrated' to a lower energy position in an adjacent interstitial location. This effect is responsible for the anomalous data points on the graph in an earlier publication [9] relating interstitial formation energies to excess interstitial volume, and the revised version of this figure is presented here.

Starting from a specific relaxed configuration, dimer calculations were performed to determine the energies, saddle points, and final configurations of all the possible transitions from that configuration. To study He–core interactions dynamically, MD simulations were performed for up to 8 ps at 100 K for single migrating He atoms near the edge dislocation core on both the tension and compression sides of the slip plane. To study the effects of different Fe–Fe potentials on He–dislocation interactions, separate test cells were constructed for the Ackland and Mendelev Fe–Fe potentials because their equilibrium lattice parameters for perfect Fe are slightly different, see Table 1.

2.5. Grain boundaries

The procedure for computing the atomic arrangements of GBs and the effect of such arrangements on the binding of interstitial and substitutional He has been described in detail elsewhere [8,21,22] so only salient details will be presented here. The computational model consists of a two-part rectangular cell in which a movable array of atoms is embedded in a semi-rigid array of atoms. The GB bisects the model and is periodic in the plane of the GB. Four symmetric tilt GBs were studied in this work, all with a common $\langle 1\,0\,1\rangle$ tilt axis. The four GBs were $\Sigma 3\{1\,1\,2\}$ $\Theta = 70.53°$, $\Sigma 11\{3\,2\,3\}$ $\Theta = 50.48°$, $\Sigma 9\{1\,1\,4\}$ $\Theta = 38.94°$, and $\Sigma 3\{1\,1\,1\}$ $\Theta = 70.53°$.

Ground state (minimum energy) structures for each GB were determined by computing the γ-surface. This was accomplished by macroscopically translating one grain relative to the other and relaxing the system using molecular dynamics with an energy quench. Atoms in the movable array were free to move, but only rigid-body displacements normal to the GB plane were allowed. Local minima on the γ-surface were then fully relaxed, which included both local atomic displacements and 3D rigid-body translations of each grain. Once the ground state structures for each GB were determined, the GB energy was carefully computed along with the variation of excess atomic volume normal to the GB plane.

Binding of He to each GB was investigated by inserting a single interstitial or substitutional He atom, and then fully relaxing the simulation block again. A relatively large number of initial positions for He atoms were studied to determine the dependence of He binding energy on the distance from the GB plane.

The transition states and mechanisms for migration of interstitial He in two representative GBs. i.e. $\Sigma 3\{1\,1\,2\}$ and $\Sigma 11\{3\,2\,3\}$, were studied by the dimer method. Periodic 'boundary conditions' were employed parallel to the GB plane, whereas a fixed 'boundary condition' was applied in the direction normal to the GB. The shape of the computational block was rectangular with dimensions of $\sim 33 \times 36 \times 32$ Å for both GBs. The dimer separation was set at 10^{-3} Å, and the value of the finite difference step for both rotation and translation was 10^{-4} Å. A maximum move distance for the dimer was initially set at 0.1 Å, as used previously for self-interstitials in Fe [23], but this value gave small rates of success in finding saddle points. Decreasing the maximum move distance to 0.01 Å was found to yield higher success rates ($\sim$80%). The dimer search is stopped when the total force for all atoms in the model is less than 10^{-4} eV/Å. For each initial state we generally carried out 50 dimer searches with initial dimer vectors, which were generated randomly to have nonzero components only on 10–30 atoms around a He interstitial.

2.6. Particle–matrix interfaces

The effect of particle elastic properties on the binding of He–vacancy clusters to the particle–matrix interface was investigated by embedding coherent, 2 nm diameter, particles in a large 3D periodic computational cell of Fe. A cubic computational cell was used with a repeat distance of 50 lattice parameters on each side. A computational cell of these dimensions contained about 250 000 atoms. Coherent particles were introduced by switching the chemical identities of 339 atoms from Fe to either Cu or modified Cu at the center of the computational cell. Fig. 3 shows a section through the middle of a Cu particle embedded in Fe. Only a few Fe atoms are plotted to illustrate the nature of the particle–matrix interface. Note the surface of the particle is not spherical but faceted.

As shown in Table 1, normal Cu particles are elastically stiffer than Fe, and particles formed from modified Cu are elastically softer than Fe. Since all the particles were intended to be coherent, they were constrained to adopt the bcc crystal structure of Fe. In all cases the particles have positive misfits because the lattice parameters of our bcc Cu and modified Cu are approximately equal to each other and larger than bcc Fe. Thus, during relaxation the particle seeks to expand against the surrounding Fe matrix, but is constrained by it. To make the relaxation process more efficient we adjusted the cell volume prior to relaxation by applying a volumetric strain to our models that was estimated from $\Delta V/V \sim (1 + \varepsilon_{xx} + \varepsilon_{yy} + \varepsilon_{zz}) \sim N_P(\Omega_P - \Omega_{Fe})$ where $\Delta V/V$ is the volume strain, ε_{xx}, ε_{yy}, and ε_{zz} are principal strains, N_P is the number of atoms in the particle, and Ω_P, Ω_{Fe} are the atomic volumes of a particle atom (bcc phase) and an Fe atom, respectively. Once the model was prepared as described above, the various He_mV_n complexes ($m = 0,1, n = 1,2$) were inserted at different distances from the Fe/particle interface to explore the spatial dependence of the

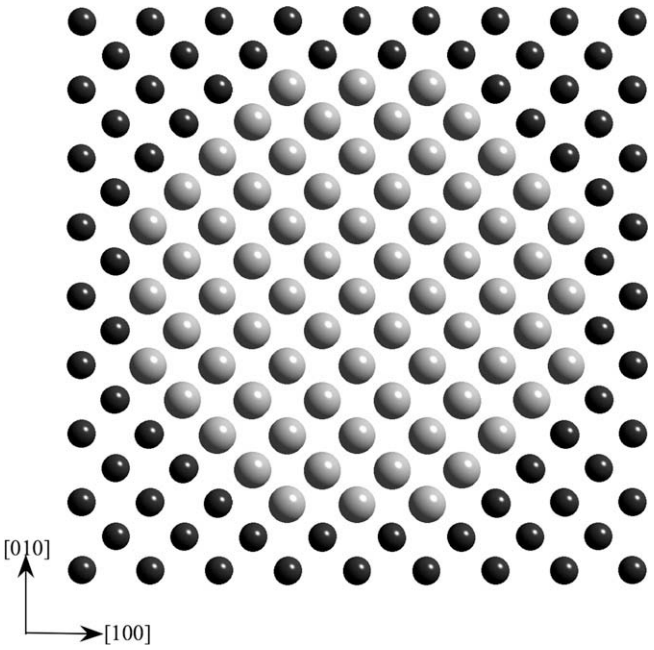

Fig. 3. Section through center of a 2 nm coherent Cu particle (gray atoms) embedded in an Fe matrix (black atoms). Note only a few Fe atoms are shown to illustrate the nature of the particle/matrix interface. The [0 0 1] direction is normal to the page.

He–vacancy complex interaction with the particle. A conjugate gradient relaxation scheme was used to relax our models. The cell volume was adjusted during relaxation by calculating the Virial pressure and applying a uniform volumetric strain to zero the pressure.

3. Results and discussion

3.1. Binding of He to dislocations

The binding energies of substitutional and interstitial He atoms to edge and screw dislocations were calculated as a function of the location of the He relative to the center of the dislocation. The calculated results of binding energies of interstitial He atoms as a function of distance from the edge and screw dislocations are discussed in detail elsewhere [9,24]. The binding and migration energies are summarized in Table 2. The binding energies are very position dependent, and only maximum binding energies are reported in the table. In general, both substitutional and interstitial He atoms are more strongly bound to the edge dislocation than to the screw. For both dislocation types the binding energy drops off sharply for He atoms at greater than about 0.5 nm from the center of the dislocation core.

Using the Ackland potential for Fe–Fe interactions, the most stable interstitial He configuration is in the octahedral location. However, near the edge dislocation where its binding energy is maximum, the He atom assumes a crowdion configuration in the close-packed [1 1 1] direction that is perpendicular to the dislocation line in the direction of the Burgers vector. Fig. 4 is a plot of the binding energy as a function of the excess interstitial volume for a He interstitial at a number of locations in and near the edge dislocation core. There appears to be a direct correlation between the excess interstitial volume and the binding energy of the He interstitial, with a distinct threshold for the formation of the crowdion configuration. He interstitials near the screw dislocation are never observed in the crowdion configuration. This is probably because the excess interstitial volume in the vicinity of the screw dislocation is not sufficient to promote the formation of the crowdion, although the different symmetries of the edge and screw displacement fields may also have an effect.

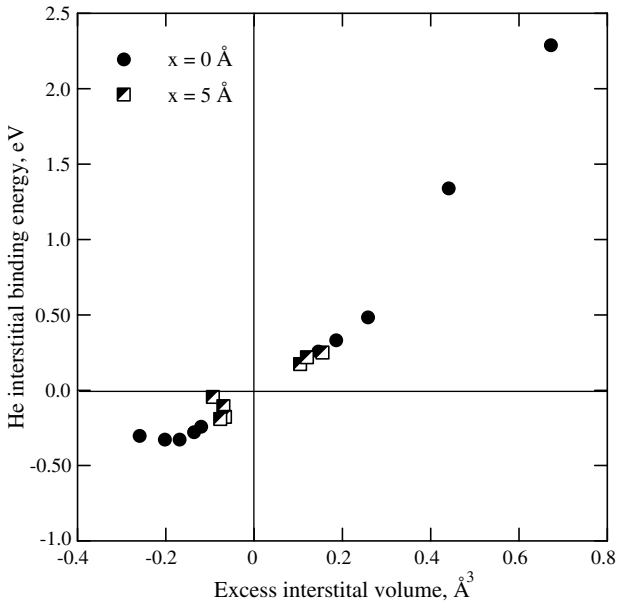

Fig. 4. The binding energies in eV of interstitial He atoms to an $(a/2)\langle 1\,1\,1\rangle\{1\,1\,0\}$ edge dislocation in α-Fe as a function of excess interstitial volume in Å^3 (1 Å^3 $\sim 0.1\ \Omega_{Fe}$) in and near the dislocation core. At locations at which the He atoms have binding energies greater than about 1.25 eV the interstitial He is in a crowdion configuration, otherwise it remains as an octahedral interstitial. The circles are for locations along a line normal to the slip plane through the center of the dislocation, while the square symbols refer to locations along a line parallel to that and displaced 0.5 nm from the core.

Table 3
Effect of GB structure and excess volume on binding energies of interstitial and substitutional He in Fe

Grain boundary	GB energy (J/m^2)	Excess vol./GB area (Å)	Maximum interstitial binding energy (eV)	Maximum substitutional binding energy (eV)
Σ3{1 1 2}	0.30	0.066	0.55	0.17
Σ11{3 2 3}	1.05	0.216	1.40	0.42
Σ9{1 1 4}	1.40	0.357	2.29	0.70
Σ3{1 1 1}	1.51	0.408	2.66	0.78

3.2. Binding of He to grain boundaries

Our results for binding energies of interstitial and substitutional He at four ⟨1 1 0⟩ symmetric tilt GBs in Fe have been reported previously [8]. Table 3 summarizes the results of our calculations. The GBs we selected to study were intended to span a relatively wide range of structures with attendant variation in GB energies and excess volumes. It is evident from the data in Table 3 that there is a strong correlation between GB energy and excess volume. Similar correlations have been observed for both fcc and bcc metals in which symmetric and asymmetric tilt GBs as well as symmetric and asymmetric twist GBs were investigated [25]. This correlation was not sensitive to the type of interatomic potential employed (i.e., Lennard-Jones versus many-body potentials) [25]. Binding energies of He atoms to GBs are defined here in the same way as for dislocations, namely, the difference in formation energy of the interstitial or substitutional He atom in or near the GB minus the formation energy of the same defect in perfect bulk Fe. In our simulations we found that He binding energies depend sensitively on the precise location of the He atom within and normal to the GB plane, so for simplicity, only maximum binding energies are presented in Table 3. As noted previously [8] there is a clear dependence of the maximum binding energy for both interstitial and substitutional He on GB excess volume. The same general trend of increasing binding energy associated with increasing excess volume found for dislocations is also observed for GBs. Thus, low-energy–low-excess volume GBs are less likely to form bubbles since He atoms are weakly bound to such boundaries and can diffuse away at moderate temperatures. On the other hand, high-energy–high-excess volume GBs are much more potent traps for He and consequently are much more likely to nucleate and grow bubbles. Experimental evidence for this has been reported in the literature [26]. Thorsen et al. [26] measured the sizes of bubbles

Table 2
Effect of dislocation character on binding and migration energies for interstitial and substitutional He in Fe

Configuration	Maximum binding energy (eV)	Migration energy (eV)
Interstitial He in perfect Fe	–	0.08
Interstitial He in edge dislocation core	2.29	0.4–0.5 Along core
Interstitial He in screw dislocation core	1.05	0.4–0.5 Along core
Substitutional He in edge dislocation core	0.50	–
Substitutional He in screw dislocation core	0.25	–

at 55 GBs in He-implanted Cu specimens. They discovered that low-energy boundaries contained smaller bubbles than high-energy boundaries, and that medium energy boundaries tended to contain medium size bubbles [26]. They attributed the bubble size distribution on increasing He diffusivity with increasing GB energy rather than increased binding to GBs with greater excess volume. Based on limited data presented below on the migration of interstitial He in two GBs with significantly different energies we do not find evidence for increased He diffusivity with increasing GB energy, but we need to investigate a wider range of GBs before definitive conclusions can be reached.

3.3. Binding of He to particle–matrix interfaces

Fig. 5 shows the interaction energy between either a single vacancy (V_1) or a substitutional He atom (He_1V_1) as a function of their distance from a 2 nm diameter coherent bcc Cu particle. The dependence of vacancy and He binding on interface character was explored by placing mono-vacancies or substitutional He atoms at different distances from either the (100) or (101) face of the Cu particle. In this case the elastic properties of the bcc Cu particle are stiffer than bcc Fe as shown in Table 1. The calculated binding energies for mono-vacancies and substitutional He at the interface were nearly the same at ~0.58 eV. The distance dependence of the interaction energy for both types of point defects was also nearly the same, and no significant effect of interface character was found. To a first approximation the binding energies are roughly equal to the defect formation energy in bcc Fe minus the defect formation energy in bcc Cu. From Table 1 the predicted binding energies for a mono-vacancy and a substitutional He atom are 0.38 eV and 0.71 eV, respectively. It should be noted that the defect formation energies given in Table 1 are computed for the pure metals at zero temperature and pressure, hence, they will be different from the defect formation energies in the Cu particle and in Fe near the particle because of the compressive stress states that exists in these regions.

Fig. 6 presents the defect-particle interaction energy results for both di-vacancies (V_2) and He/di-vacancy complexes (He_1V_2) in the vicinity of a 2 nm coherent Cu particle. Both first nearest neighbor

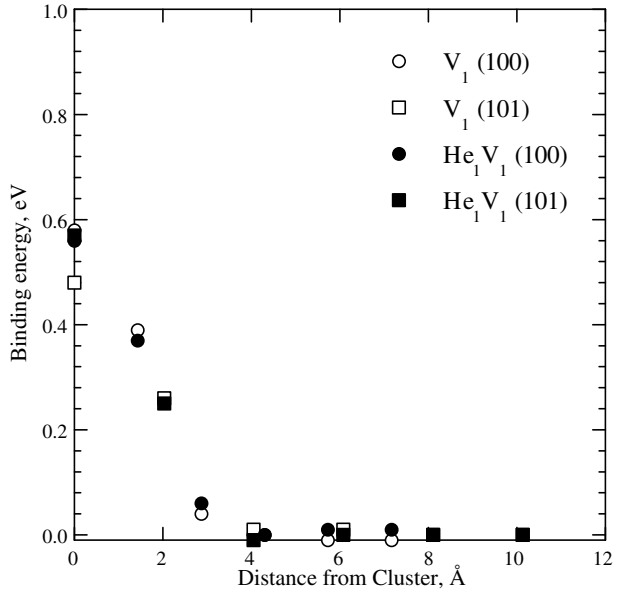

Fig. 5. The interaction energy between a single vacancy (V_1), or a substitutional He atom (He_1V_1) and a 2 nm coherent bcc Cu particle in Fe as a function of the distance from either the (100) or (101) face of the Cu cluster. The particle is elastically stiffer than Fe.

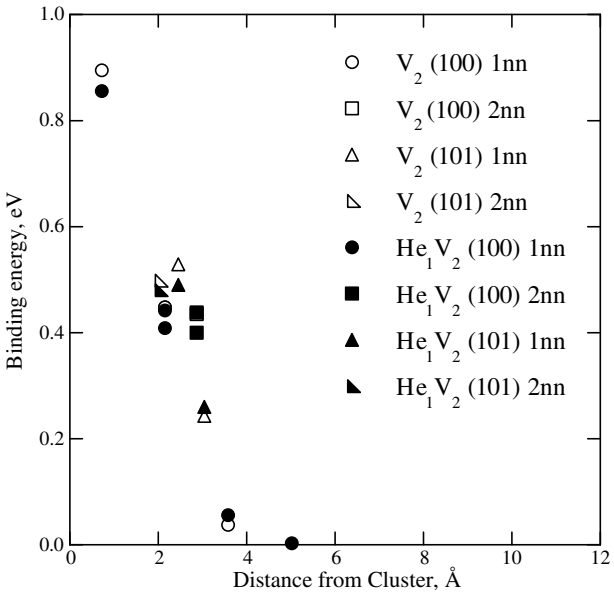

Fig. 6. The interaction energy between a di-vacancy (V_2), or a He/di-vacancy (He_1V_2) complex as a function of distance from a 2 nm coherent bcc Cu particle in Fe. Di-vacancy configurations are either first nearest neighbor (1nn) or second nearest neighbor (2nn). The particle is elastically stiffer than Fe.

(1nn) and second nearest neighbor (2nn) di-vacancy configurations were considered. The dependence of binding energy on interface character was also examined and found to be not significant. The binding energies of di-vacancies and He/di-vacancy complexes were nearly the same at ~0.85 eV near the interface. Similar to the mono-vacancy and substitutional He, the binding energy for di-vacancies and He/di-vacancy complexes can be predicted from the difference in their defect formation energies in Fe and Cu. For 1nn V_2 and He_1V_2 defects the binding energies predicted from the data in Table 1 are 0.84 and 1.07 eV, respectively. Similarly, for 2nn V_2 and He_1V_2 defects the predicted binding energies are 0.67 and 1.03 eV, respectively. The predicted binding energies are fairly close to the calculated value, which is somewhat unexpected given that these defects simultaneously reside in both the Cu particle and in the Fe matrix.

Figs. 7 and 8 display results analogous to those shown in Figs. 5 and 6 except that the particles were formed from modified Cu with elastic constants softer than Fe. Note the cohesive energy for the modified fcc Cu phase is the same as normal fcc Cu, but the cohesive energy of the modified bcc phase is about 0.1 eV greater than normal bcc Cu. The larger cohesive energy of a single vacancy in the modified bcc Cu may partially account for the 0.35 eV increase in the mono-vacancy formation energy. The results clearly show that vacancies and He–vacancy complexes are more weakly bound to the modified Cu particles. In addition, mono-vacancy binding energies (0.28–0.35 eV) were lower than substitutional He binding energies (0.39–0.49 eV). The defect formation energy data given in Table 1 suggest this trend. The vacancy formation energy in modified Cu is only 0.03 eV smaller than Fe, so weaker binding of mono-vacancies is expected. Similarly, the substitutional He formation energy in modified Cu is 0.13 eV greater than in normal Cu, so weaker binding would be anticipated. Further, the differences in defect formation energies suggest that substitutional He atoms would be bound more strongly than single vacancies to modified Cu particles as shown in Fig. 7. Di-vacancies and He_1V_2 complexes were also more weakly bound to the modified Cu particle, which results from increased defect formation energies in modified Cu relative to normal Cu, see Table 1. Differences in defect formation energy predict that di-vacancies should be more

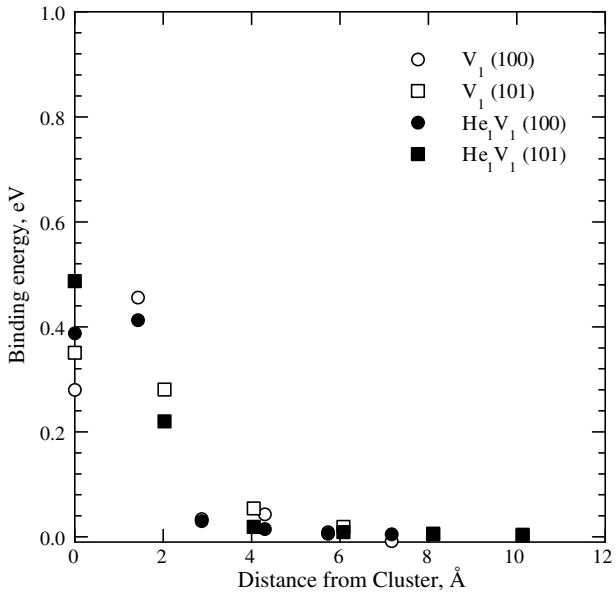

Fig. 7. The interaction energy between a single vacancy (V_1), or a substitutional He atom (He_1V_1) as a function of distance from a 2 nm modified Cu particle in Fe. The particle is elastically softer than Fe.

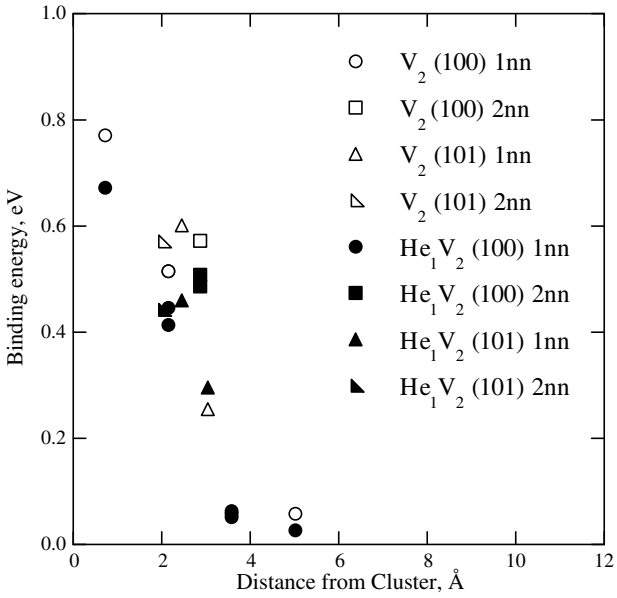

Fig. 8. The interaction energy between a di-vacancy (V_2), or a He/di-vacancy (He_1V_2) complex as a function of distance from a 2 nm modified Cu particle in Fe. Di-vacancy configurations are either first nearest neighbor (1nn) or second nearest neighbor (2nn). The particle is elastically softer than Fe.

weakly bound to the nanocluster than He_1V_2 complexes, but the results displayed in Fig. 8 indicate the opposite was observed.

3.4. Migration of He within and near the core of a dislocation

Migration energies of He atoms near and within the dislocations are obtained using the dimer analysis, from which the saddle point energies and atom configurations of the transition states involved in migration can be determined.

3.4.1. Interstitial He–edge dislocation

As expected, interstitial He atoms approaching the core region on the tensile side of the edge dislocation migrate more favorably toward the dislocation line than away from it. In all dimer trials the He atom is initially placed in an octahedral interstitial site, but during the initial relaxation of the dimer process it may assume a different pre-transition configuration. For the edge dislocation, an octahedral interstitial He placed about three Burgers vectors from the dislocation center on the tensile side migrates toward the center with a migration energy on the order of 0.2 eV, remaining in octahedral sites. Closer to the dislocation, as excess volume increases, the relaxed He atom is more likely to occupy tetrahedral interstitial sites, and very near and within the dislocation core, the lowest energy interstitial configuration for a He atom on the tensile side is a [1 1 1] crowdion. The region about the dislocation in which He is most stable as a crowdion has an oval-like cross section extending about 0.8 nm on either side of the dislocation line and about 0.8 nm above the slip plane. This is similar to the interaction region of a self-interstitial Fe atom with an edge dislocation determined by Kuramoto et al. [27], which is consistent with the shape of the tensile strain field of the dislocation.

Within the edge dislocation core, a He atom in the crowdion configuration preferentially migrates along the dislocation line, which is perpendicular to the crowdion direction, by hopping to crowdion positions in adjacent rows with a migration energy of 0.4–0.5 eV, depending on the initial position. He migration energies near and within dislocations are summarized in Table 2. The activation energy for He jumping out of the crowdion configuration to an octahedral interstitial site (as a first step of migrating away from the dislocation) is about 1.5 eV. He atoms placed in the model on the compression side of the edge dislocation, at locations greater than a lattice parameter from the center of the dislocation, remain in octahedral sites upon relaxation and migration. Migration energies are on the order of 0.25 eV toward the dislocation and 0.02 eV away from the dislocation, consistent with having negative binding to the compression side of the dislocation.

3.4.2. Interstitial He–screw dislocation

The binding energy of an interstitial He atom to the $(a/2)\langle 1\,1\,1\rangle$ screw dislocation in Fe is about 1.0 eV, or about half that of interstitial He to the $(a/2)\langle 1\,1\,1\rangle\{1\,1\,0\}$ edge dislocation. However, the circular cross-sectional area about the screw dislocation within which interstitial He is significantly attracted toward the core is about the same as the cross-sectional area of the attractive region about the edge dislocation. No He atoms were observed to relax into the crowdion configuration anywhere in or near the screw dislocation in Fe.

Despite the factor-of-two differences in formation energies of He interstitials near the edge and screw dislocations, the migration energy ranges for He undergoing 'pipe diffusion' along the dislocation cores of both types of dislocation are about the same, 0.4–0.5 eV. However, the excess interstitial volume in the core region is significantly greater in the edge dislocation than in the screw, and the migration mechanisms of He in the two dislocation cores are quite different, with interstitial He atoms migrating in the crowdion configuration along the edge and as octahedral interstitials along the screw.

3.5. Migration of He in grain boundaries

Initially, the lowest energy configuration of a single He interstitial within each GB was determined by annealing the computational cell at 1000 K for about 10 ps and then slowly cooling down to 0 K. These stable configurations were used as the initial states for investigating migration of He interstitials using the dimer method. The most stable configuration of a He interstitial in the $\Sigma 3$ GB is located mid-way between two Fe atoms along the [1 1 0] direction, but slightly displaced along the $[1\,\bar{1}\,1]$ direction, as shown in Fig. 9. However, in the $\Sigma 11$ GB the most stable config-

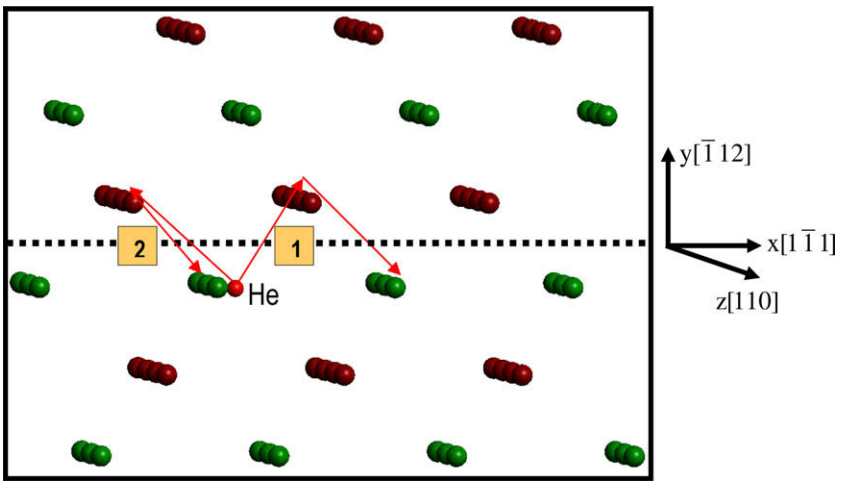

Fig. 9. Atomic plots showing two different paths of interstitial He migration in the Σ3{112} GB. Path 1 is along the [1$\bar{1}$1] direction, and path 2 is along the [110] direction. Bright red spheres indicate He atom positions, while dark red and green spheres represent Fe atoms in alternating {110} planes perpendicular to the ⟨110⟩ tilt axis. Note the model has been rotated slightly about the [$\bar{1}$12] direction. (For interpretation of the references in colour in this figure legend, the reader is referred to the web version of this article.)

uration of a He interstitial is located at the middle of two triangles, each formed by three Fe atoms on the same plane normal to the [110] direction (octahedral position), and its structure is detailed in Fig. 10. Dimer searches generally identify a number of transition states, but the most likely migration paths are those with the lowest energy barriers. In the Σ3 GB, two possible migration paths for interstitial He were discovered, as shown in Fig. 9, which are likely the most common diffusion mechanisms in this GB. In Fig. 9, the He interstitial crosses the GB plane (dotted line) to an atomic row in the upper grain. Its final position is equivalent to its initial configuration, but on a different atomic plane (path 1). The arrow in Fig. 9 indicates the migration path of the He atom, and the corresponding energy barrier is about 0.47 eV, which is much higher than interstitial He in bulk Fe. From this position, the He atom is able to cross the GB again and return to its starting point in the lower grain. The saddle point energy for this second move is essentially the same as for the first jump, 0.46 eV. If its final position is similar to the original position in the next atomic row, then this will lead to the migration of the He atom along the [1$\bar{1}$1] direction. A sequence of moves of this type is given in Fig. 9. However, if the final position of the He atom is in the same atomic row as that of its original position, this will lead to the migration of the He atom along the [110] direction, as shown in Fig. 9 (path 2). Because these paths have the same energy barrier, the He interstitial can migrate two-dimensionally on the GB plane at low temperatures. The next lowest energy barrier obtained from dimer searches is about 0.68 eV, which is associated with the migration of the He atom away from the GB. This leads to dissociation of the He atom from the GB, and results in 3 D diffusion at higher temperatures, which is consistent with the small binding energy to the Σ3 GB. Previously, MD simulations were employed to study He diffusion in the Σ3 GB [10], and it was found that interstitial He atoms migrate two-dimensionally at low temperatures and three-dimensionally at higher temperatures. The present results obtained by the dimer searches are in good agreement with the long-time MD simulations.

Unlike the migration of interstitial He within the Σ3 GB, only one migration path has been observed with 50 dimer searches for the Σ11 GB, which is shown in Fig. 10. The most stable position of the He interstitial is an octahedral site below or above the GB plane, as indicated by a dotted line in Fig. 10. The He atom can migrate from an octahedral position below the GB plane to an equivalent position above the GB plane with an energy barrier of about 0.47 eV, but further movement of the He atom along the same direction is not observed. Due to strong binding to this GB, the He atom prefers to change its direction, and migrates back to the octahedral position below the GB plane. The arrows in Fig. 10 indicate the lowest energy path of the He atom within the Σ11 GB, and

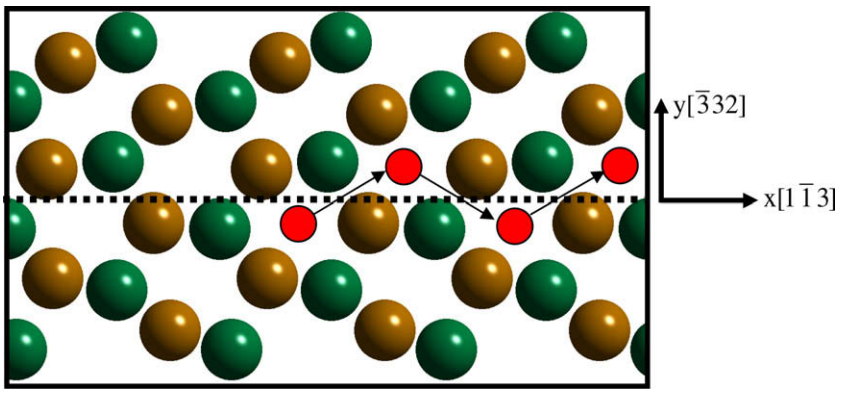

Fig. 10. An atomic plot illustrating the 1D zigzag migration path of interstitial He atoms in the Σ11{323} GB. Bright red spheres show He atom positions, while gold and green spheres represent Fe atoms in alternating {110} planes perpendicular to the ⟨110⟩ tilt axis. Note the [110] direction is perpendicular to the plane of the paper. (For interpretation of the references in colour in this figure legend, the reader is referred to the web version of this article.)

this path leads to the He atom migrating one-dimensionally along the interface, but with zigzag behavior. The migration energy in the $\Sigma 11$ GB is very similar to that determined for the $\Sigma 3$ GB, but the trajectories are different, resulting in different migration behaviors. Also, the diffusion of a He interstitial in the $\Sigma 11$ GB has been investigated by long-time MD simulation [10], and the results show that the He interstitial migrates one-dimensionally along the $[1\,\bar{1}\,3]$ direction, even at high-temperatures. The present results are in general agreement with those observed in the MD simulations, which suggests that the migration mechanisms of a He interstitial depend on GB structure and binding energy. These results demonstrate that different migration mechanisms of a He interstitial, especially affecting the dimensionality of migration, may have a significant effect on He bubble nucleation in different GBs.

4. Summary and conclusions

Our results clearly show that interstitial He is strongly bound to both dislocations and GBs with maximum binding energies ranging from 0.55 to 2.66 eV. Substitutional He is also bound to dislocations and GBs, but much more weakly than for interstitial He, with maximum binding energies between 0.17 and 0.78 eV. All point defect complexes considered in this study are bound to positive misfit, 2 nm particles embedded in an Fe matrix with binding energies ranging from 0.50 to 0.58 eV for single vacancies and substitutional He atoms. Di-vacancies and He/di-vacancy complexes are more strongly bound with binding energies of ~0.85 eV. Point defects are not as strongly bound to particles elastically softer than Fe when compared to particles elastically stiffer than Fe. To first order, differences in point defect formation energies are likely responsible for the binding energies observed.

Binding energies strongly correlate with defect excess volume. Consequently edge dislocations are stronger He traps than screw dislocations because of the much larger excess volume available in an edge dislocation compared with a screw dislocation. Helium trapping at GBs is somewhat greater to somewhat less than for dislocations depending on the type of GB. Coherent, positive misfit, nanoparticles also efficiently trap He, but semi-coherent particles may be more efficient traps because of the excess volume associated with the array of misfit dislocations needed to accommodate the lattice parameter mismatch between the particle and matrix.

Interstitial He migrates along the $\langle 1\,1\,2\rangle$ edge dislocation line within a 'ribbon' about 2 nm wide with a minimum cross section of about 2 nm^2. Migration of He interstitials along the $\langle 1\,1\,1\rangle$ screw dislocation occurs within a cylinder of about 2 nm in diameter. Pipe diffusion of interstitial He is approximately the same for pure edge and pure screw dislocations with migration energies of about 0.4–0.5 eV in both cases. For the two GBs we have studied the migration energies of interstitial He in GBs determined by both dimer and long-time MD calculations were similar to those for dislocations at about ~0.4–0.5 eV. Dimer calculations also show that the dimensionality of interstitial He migration depends on GB structure even though migration energy does not. Such differences in migration dimensionality may have significant implications for He bubble nucleation and growth.

Acknowledgement

This research is supported by the US Department of Energy, Office of Fusion Energy Sciences, under Contract DE-AC06-76RLO 1830.

References

[1] S. Jitsukawa, A. Kimura, A. Kohyama, R.L. Klueh, A.A. Tavassoli, B. van der Schaaf, G.R. Odette, J.W. Rensman, M. Victoria, C. Petersen, J. Nucl. Mater. 39 (2004) 329.
[2] D.L. Smith, S. Majumdar, M. Billone, R. Mattas, J. Nucl. Mater. 716 (2000) 283.
[3] H. Schroeder, P. Batfalsky, J. Nucl. Mater. 117 (1983) 287.
[4] I.-S. Kim, J.D. Hunn, N. Hashimoto, D.L. Larson, P.J. Maziasz, K. Miyahara, E.H. Lee, J. Nucl. Mater. 280 (2000) 264.
[5] B.D. Wirth, G.R. Odette, J. Marian, L. Ventelon, J.A. Young-Vandersall, L.A. Zepeda-Ruiz, J. Nucl. Mater. 103 (2004) 329.
[6] K. Morishita, R. Sugano, B.D. Wirth, J. Nucl. Mater. 323 (2003) 243.
[7] K. Morishita, R. Sugano, B.D. Wirth, T. Diaz de la Rubia, Nucl. Instrum. and Meth. B 202 (2003) 76.
[8] R.J. Kurtz, H.L. Heinisch, J. Nucl. Mater. 1199 (2004) 329.
[9] H.L. Heinisch, F. Gao, R.J. Kurtz, E.A. Le, J. Nucl. Mater. 351 (2006) 141.
[10] F. Gao, H.L. Heinisch, R.J. Kurtz, J. Nucl. Mater. 351 (2006) 133.
[11] G.J. Ackland, D.J. Bacon, A.F. Calder, T. Harry, Philos. Mag. A 75 (1997) 713.
[12] W.D. Wilson, R.D. Johnson, Interatomic Potential and Simulation of Lattice Defects, Plenum, 1972. p. 375.
[13] D.E. Beck, Mol. Phys. 14 (1968) 311.
[14] M.I. Mendelev, S. Han, D.J. Srolovitz, G.J. Ackland, D.Y. Sun, M. Asta, Philos. Mag. 83 (2003) 3977.
[15] T. Seletskaia, Y. Osetsky, R.E. Stoller, G.M. Stocks, Phys. Rev. Lett. 94 (2005) 046403.
[16] C. Fu, F. Willaime, Phys. Rev. B 72 (2005) 064117.
[17] T. Seletskaia, Y. Osetsky, R.E. Stoller, G.M. Stocks, J. Nucl. Mater. 351 (2006) 109.
[18] G. Voronoi, J. Reine Angew. Math. 134 (1908) 198.
[19] G. Henkelman, H. Jónsson, J. Chem. Phys. 111 (1999) 7010.
[20] G. Mills, H. Jónsson, G.K. Schenter, Surf. Sci. 324 (1995) 305.
[21] R.J. Kurtz, R.G. Hoagland, J.P. Hirth, Philos. Mag. A 79 (1999) 665.
[22] R.J. Kurtz, R.G. Hoagland, J.P. Hirth, Philos. Mag. A 79 (1999) 683.
[23] F. Gao, G. Henkelman, W.J. Weber, L.R. Corrales, H. Jónsson, Nucl. Instrum. and Meth. B 202 (2003) 1.
[24] H.L. Heinisch, F. Gao, R.J. Kurtz, J. Nucl. Mater. 367–370 (2007) 311.
[25] D. Wolf, K.L. Merkle, in: D. Wolf, S. Yip (Eds.), Materials Interfaces: Atomic Level Structure and Properties, first ed., Chapman & Hall, London, 1992, p. 87.
[26] P.A. Thorsen, J.B. Bilde-Sorensen, B.N. Singh, Scr. Mater. 51 (2004) 557.
[27] E. Kuramoto, K. Ohsawa, T. Tsutsumi, J. Nucl. Mater. 778 (2000) 283.